LA-UR-18-28615 (Accepted Manuscript)

Light-Emitting Metasurfaces: Simultaneous Control of Spontaneous Emission and Far-Field Radiation

Liu, Sheng; Vaskin, Aleksandr; Addamane, Sadhvikas; Leung, Benjamin; Tsai, Miao-Chan; Yang, Yuanmu; Vabishchevich, Polina; Keeler, Gordon; Wang, George; He, Xiaowei; Kim, Younghee; Hartmann, Nicolai; Htoon, Han; Doorn, Stephen K.; Zilk, Matthias; Pertsch, Thomas; Balakrishnan, Ganesh; Sinclair, Michael; Staude, Isabelle; Brener, Igal

To be published in: Nano Letters

DOI to publisher's version: 10.1021/acs.nanolett.8b02808

Permalink to record: http://permalink.lanl.gov/object/view?what=info:lanl-repo/lareport/LA-UR-18-28615

NANO LETTERS
Cite This: Nano Lett. XXXX, XXX, XXX−XXX
Letter
pubs.acs.org/NanoLett

Light-Emitting Metasurfaces: Simultaneous Control of Spontaneous Emission and Far-Field Radiation

Sheng Liu,[†,§] Aleksandr Vaskin,[‡] Sadhvikas Addamane,[⊥] Benjamin Leung,[†] Miao-Chan Tsai,[†] Yuanmu Yang,[†] Polina P. Vabishchevich,[†,§] Gordon A. Keeler,[†] George Wang,[†] Xiaowei He,[∥] Younghee Kim,[∥] Nicolai F. Hartmann,[∥] Han Htoon,[∥] Stephen K. Doorn,[∥] Matthias Zilk,[‡] Thomas Pertsch,[‡] Ganesh Balakrishnan,[⊥] Michael B. Sinclair,[†] Isabelle Staude,[‡] and Igal Brener*[,†,§]

[†]Sandia National Laboratories, Albuquerque, New Mexico 87185, United States
[‡]Institute of Applied Physics, Abbe Center of Photonics, Friedrich Schiller University Jena, 07745 Jena, Germany
[§]Center for Integrated Nanotechnologies, Sandia National Laboratories, Albuquerque, New Mexico 87185, United States
[⊥]Center for High Technology Materials (CHTM), University of New Mexico, Albuquerque, New Mexico United States
[∥]Center for Integrated Nanotechnologies, Materials Physics and Applications Division, Los Alamos National Laboratory, Los Alamos, New Mexico 87545, United States

Supporting Information

ABSTRACT: Light-emitting sources and devices permeate every aspect of our lives and are used in lighting, communications, transportation, computing, and medicine. Advances in multifunctional and "smart lighting" would require revolutionary concepts in the control of emission spectra and directionality. Such control might be possible with new schemes and regimes of light−matter interaction paired with developments in light-emitting materials. Here we show that all-dielectric metasurfaces made from III−V semiconductors with *embedded* emitters have the potential to provide revolutionary lighting concepts and devices, with new functionality that goes far beyond what is available in existing technologies. Specifically, we use Mie-resonant metasurfaces made from semiconductor heterostructures containing epitaxial quantum dots. By controlling the symmetry of the resonant modes, their overlap with the emission spectra, and other structural parameters, we can enhance the brightness by 2 orders of magnitude, as well as reduce its far-field divergence significantly.

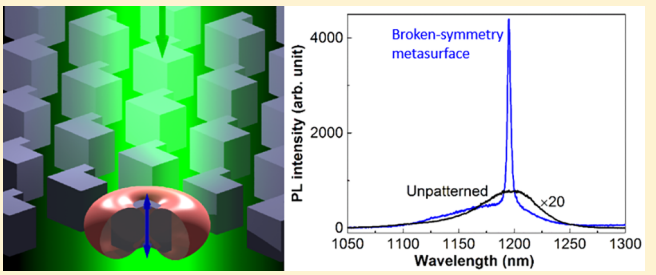

KEYWORDS: *all-dielectric nanophotonics, Mie-resonances, dielectric nanoantennas, Fourier imaging, spontaneous emission*

Improvements in our understanding of light−matter interactions have enabled a plethora of breakthroughs in light emission. Decades ago, it was realized that the spontaneous emission rate of an emitter can be manipulated by tailoring the optical density of states of its local environment.[1] Subsequently, numerous works investigated the properties of emitters coupled to Fabry−Perot cavities and optical micropillar microcavities,[2] photonic crystal cavities[3,4] as well as to systems that support high quality-factor resonances such as bound states in the continuum[5,6] and Fano resonances.[7] While Fabry−Perot cavities have been used successfully for controlling radiative rates (due to their potentially high Q-factors) and constitute the basis for commercial devices such as vertical-cavity surface-emitting lasers (VSCEL), they do not offer much possibilities for far field control beyond that offered by transverse lasing modes. In addition, they often rely on stringent epitaxial growth requirements in layer thicknesses and compositions. Lately, plasmonic[8−12] and dielectric[13,14] nanoantennas were also employed in this regard, with emitters placed in the "hot-spots" of the nanostructures to control their spontaneous emission rates. In a likewise manner, the far-field emission pattern can be controlled through coupling to nanostructured systems. For example, shaping of the far-field emission patterns from single or few localized emitters was experimentally demonstrated using plasmonic[8−12] and dielectric nanoantennas.[13,14] Metamaterials and their 2D equivalent, metasurfaces, present a new platform to control far field patterns as they provide a much more compact and often flat alternative to conventional optical components.[15−21] Over the past few years, it has been shown both theoretically and experimentally that metasurfaces can be effective for achieving far-field emission patterns with desired properties such as divergence and directionality.[10,22−26] Although both metallic and dielectric metasurfaces were used for this purpose, only an all-dielectric

Received: July 10, 2018
Revised: October 4, 2018
Published: October 19, 2018

DOI: 10.1021/acs.nanolett.8b02808
Nano Lett. XXXX, XXX, XXX−XXX

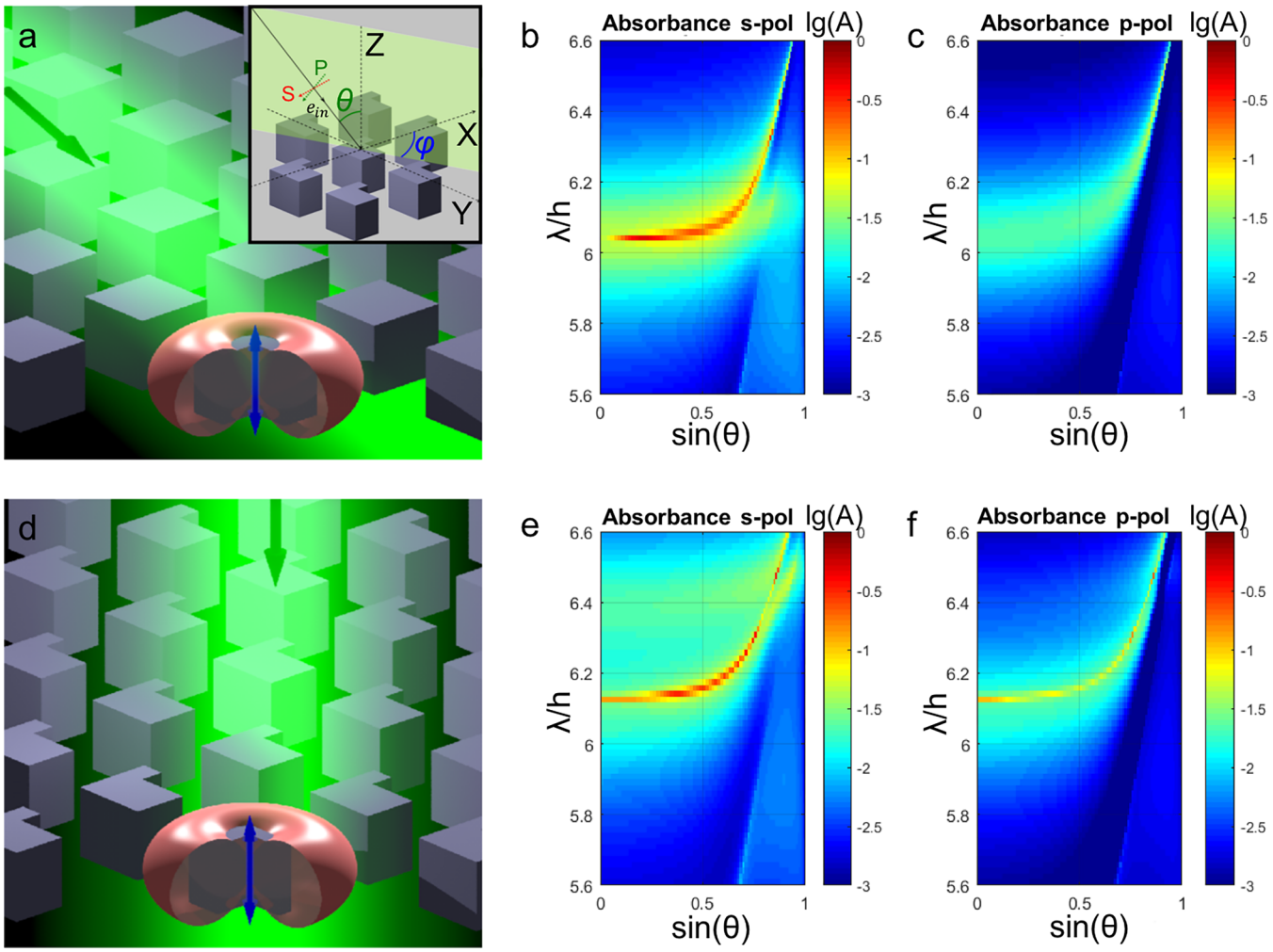

Figure 1. Modal structure of symmetric and symmetry broken semiconductor metasurfaces. (a) Sketch of a symmetric metasurface. A mode characterized by out-of-plane oriented magnetic dipole moments can be excited for oblique-incidence excitation only. The inset shows the coordinate system that denotes the directions and the angles of incidence as implied in the calculations. (b,c) Calculated absorbance spectra of the metasurface depicted in (a) for s- (TE) and p- (TM) polarized incidence light, respectively, for a variation of the polar angle θ (the azimuthal angle φ is kept equal to 0°). The out-of-plane magnetic dipole mode, which appears as a narrow band of strong absorption in (b) can only be coupled for s-polarized light. Also note that the absorption feature of this band vanishes for normal incidence. (d) Sketch of a symmetry-broken semiconductor metasurface. The symmetry break allows for excitation of the out-of-plane magnetic dipole mode at normal incidence. (e,f) Calculated absorbance spectra of the metasurface depicted in (d) for s- and p-polarized incidence light, respectively, for a variation of the polar angle θ (the azimuthal angle φ is kept equal to 0°). The out-of-plane magnetic dipole mode, now appears as a narrow band of strong absorption both for s- and p-polarized light. Additionally, the absorption feature of this band persists for normal incidence.

approach offers a low-loss platform that does not cause unnecessary loss in total quantum yield.

Past attempts at integrating emitters or other active media with metasurfaces were done in an ad-hoc and sequential manner or included inefficient emitters.[23,27,28] We have found that the full potential for emission control through exploitation of global symmetries is realized when emitters are intrinsically embedded within the metasurface constituent material. An attractive system to realize this vision is metasurfaces made from epitaxial semiconductors where high-quality quantum emitters can be incorporated during growth and top-down nanofabrication processes are readily available. Here, we show that we can achieve both goals of controlling spontaneous emission *and* far-field patterns using quantum emitters embedded within semiconductor-based all-dielectric metasurfaces, taking advantage of high-Q localized photonic modes resulting from reduced coupling to free-space and metasurface designs that control the free-space coupling to these modes.

SYMMETRY PROTECTED MODES OF DIELECTRIC METASURFACES

A starting point for understanding the behavior of arrays of high refractive index resonators is the determination of the Mie-like multipolar modes of the uncoupled resonators. (Although coupling effects occur in such arrays, for properly designed metasurfaces it is more convenient and intuitive to describe the metasurface from the standpoint of resonator modes rather than using photonic crystal formalism.[29−31]) For isolated symmetric resonators such as spheres, the properties of a multipolar mode (such as a dipole mode) are independent of its orientation. However, when the resonators are arranged in a subwavelength two-dimensional array, the properties of the modes will depend strongly on the orientation of their multipolar moments relative to the array plane. For example, electric and magnetic dipole modes oriented in the metasurface plane can be excited by normally incident waves ("bright"

DOI: 10.1021/acs.nanolett.8b02808
Nano Lett. XXXX, XXX, XXX−XXX

modes) and have low-quality (Q)-factors due to high radiation damping. In contrast, the dipole modes oriented perpendicular to the array plane cannot couple to normally propagating waves and hence exhibit very high Q-factors (Figure 1a). Such modes are known as symmetry-protected modes or dark modes.[32] The coupling to free-space waves increases as the wave vector is tilted away from the normal. Metasurface designs that feature geometrical perturbations that reduce resonator symmetry can produce weak coupling between the bright and dark resonator modes and thus offer a path for normal incidence excitation of out-of-plane magnetic and electric dipole modes.

These different families of modes with vastly different quality-factors can be leveraged for emitter radiative rate engineering. Emitters embedded in the resonators will preferentially couple to modes that possess the highest optical density of states, in this case, the high-Q, out-of-plane, symmetry protected modes. To elucidate this, we have calculated the absorption due to the excitation of the magnetic dipole modes of a subwavelength array of cubic resonators (as depicted in Figure 1a) under plane wave illumination, as a function of incidence angle for s and p polarizations. Such calculations reveal the in-plane dispersion of these modes, and by reciprocity predict their emission behavior. Details of the array geometry are provided in the Supporting Information. Figure 1b,c show that for the cube resonator array both polarizations can excite a broad in-plane dipole mode (green area). However, for s-polarization, we observe an additional, much sharper, feature that is due to the excitation of the out-of-plane magnetic dipole mode (red regions). Since the magnetic dipole emission—and by reciprocity its absorption—is forbidden along the axis of the dipole moment, the absorption band is interrupted at the center. For the broken-symmetry resonators[32] (as depicted in Figure 1d) both polarizations can couple to the high-Q vertical magnetic dipole mode at normal incidence and the absorption band is not interrupted at the center (see Figure 1e,f).

To demonstrate simultaneous control over emission rates and far-field emission profiles, two families of metasurfaces were fabricated, both containing embedded InAs epitaxial QDs.[33,34] The resonators were designed so that their lowest-order in-plane Mie modes overlapped the ground state photoluminescence of the QDs (~1.2 μm). One family included arrays of symmetrical cylindrical resonators showing broad, radiation-damped, in-plane electric and magnetic resonances; while the other family comprised arrays of broken-symmetry resonators that lead to sharp out-of-plane dipole resonances in the 1−1.3 μm spectral range. The fabrication process is shown schematically in Figure 2a and described in detail in the Methods section.[35] An electron micrograph of a typical fabricated metasurface sample composed of symmetrical cylindrical resonators is shown in Figure 2b. Epitaxial InAs dots embedded in GaAs quantum wells were chosen as the emitting species since electron confinement within the dots reduces the rate of nonradiative surface recombination.

PHOTOLUMINESCENCE FROM SYMMETRIC METASURFACES

We fabricated a series of arrays of symmetric cylindrical resonators with a constant height of 400 nm and diameters ranging from 280 to 340 nm. A constant duty cycle (defined as diameter divided by periodicity) of ~55% was used for each

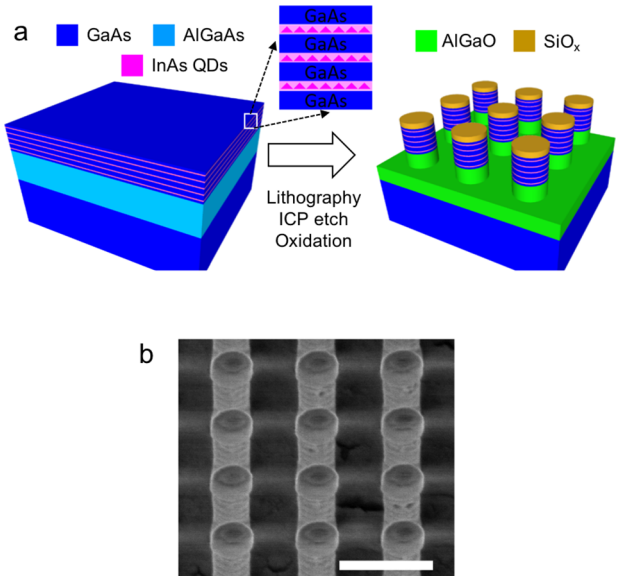

Figure 2. (a) Schematic of the III−V semiconductor wafer structure, incorporating several layers of self-assembled quantum dots in its functional layer. Using a combination of electron-beam lithography, inductively coupled plasma etching, and an oxidation procedure, the wafers are nanostructured into metasurfaces consisting of Mie-resonant nanocylinders incorporating the quantum dots. (b) Oblique-view scanning electron micrograph of a typical fabricated sample. The scale bar corresponds to 1000 nm.

array. Therefore, for each of these samples, only the ~24% of the area containing QDs remains after the samples are etched. The unpolarized photoluminescence spectra of these samples were measured using a custom-built micro− photoluminescence setup operated in reflection mode (see Methods section). Importantly, a microscope objective with a numerical aperture of 0.4 was used for the measurement, so that the emission is collected over a range of angles out to ~24 degrees. In Figure 3a, we show the measured photoluminescence spectra for several different samples of different diameters. All the photoluminescence spectra were normalized to unity. Photoluminescence from an unpatterned region is shown at the bottom (black curve).

The brightest photoluminescence is achieved for the metasurface consisting of resonators with a diameter of 320 nm. For this sample, the photoluminescence line width is quite narrow (~3 nm), and the peak intensity is ~16 times (or ~67 times considering the 24% filling fraction) stronger than the unpatterned area. The narrow line width emission and large enhancement are not compatible with the broad in-plane electric and magnetic dipole resonances, but rather are due to high-Q dark modes. We mark all the photoluminescence peaks resulting from this resonance with green arrows. As expected, the photoluminescence peaks red-shift as the resonator diameter increases. A small emission peak at ~1060 nm emerges for the 340 nm diameter resonators due to the dark magnetic quadrupole mode. Figure 3b shows the photoluminescence spectra measured from the metasurface (blue curve) together with the photoluminescence from an unpatterned sample (cyan under filled curve). Also overlaid is the reflectivity spectrum (black curve) of the metasurface. The photoluminescence emission peak at ~1200 nm spectrally coincides with the sharp minimum observed in the reflectivity. Note that this mode is observed in reflectivity due to the

DOI: 10.1021/acs.nanolett.8b02808
Nano Lett. XXXX, XXX, XXX−XXX

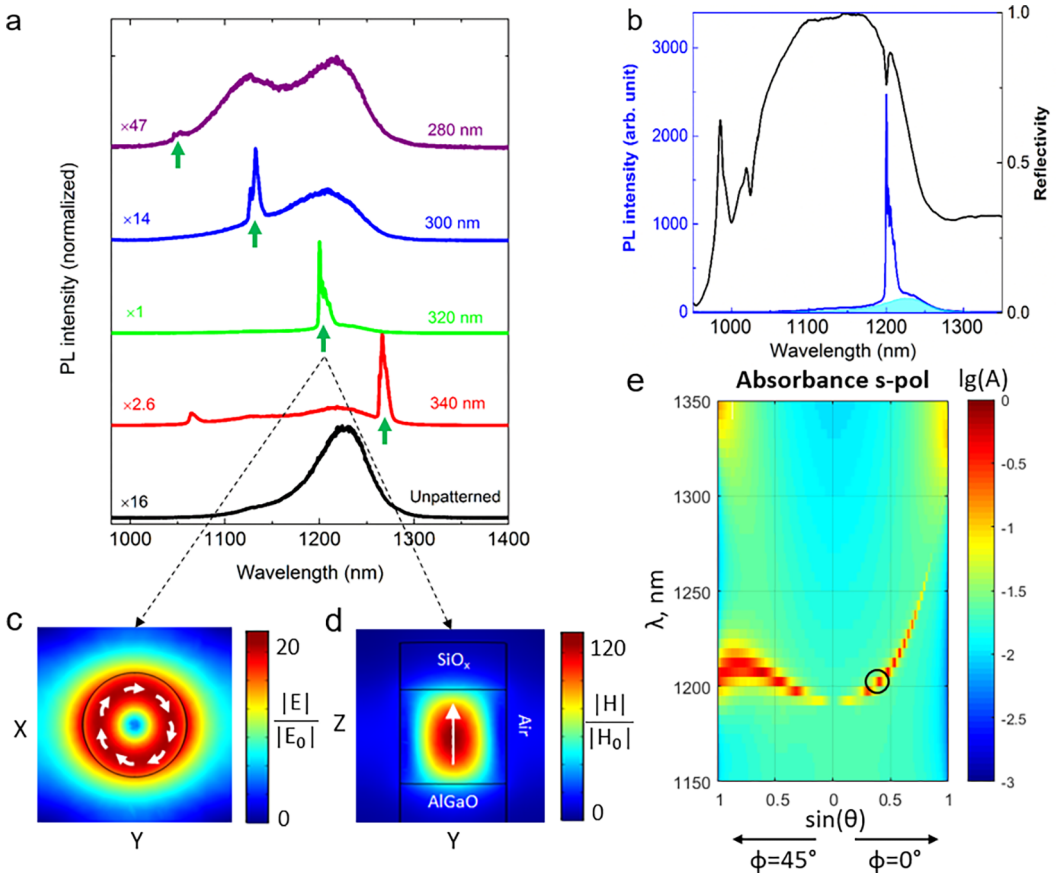

Figure 3. (a) Experimentally measured photoluminescence spectra from several symmetric metasurface samples featuring a variation of the nanocylinder diameter. The bottom curve shows the emission from the unpatterned wafer for reference. The green arrows mark the spectral positions of the different symmetry-protected, out-of-plane modes supported by the metasurface. (b) Experimentally measured linear-optical reflectance and photoluminescence spectra for the symmetric metasurface sample with a nanocylinder diameter of 320 nm, which shows the strongest brightness enhancement for the symmetric design. (c,d) Numerically calculated mode profiles (modulus of electric or magnetic fields) in a plane that cuts through the center of the nanocylinder excited by a plane wave with a wavelength of 1200 nm incident at $\theta = 20°$ and $\varphi = 0°$ for the sample with a nanocylinder diameter of 320 nm. (e) Numerically calculated angle-dependent absorbance spectra for s-polarized light. The black circle corresponds to the excitation conditions used to calculate the mode profiles in panels c and d.

angular spread of incidence angles caused by the 0.4 numerical aperture of the objective used. The measured reflection spectrum agrees well with numerical simulations (see Supplementary Figure S1). To elucidate the nature of this resonance, we show in Figure 3c,d, the simulated electric and magnetic field profiles at the peak emission wavelength in the plane that cuts through the center of the nanocylinder resonator excited by an s-polarized plane wave. This simulation was performed for a polar incidence angle θ of 20 degrees to allow coupling to the dark mode. The electric fields form a circular displacement current in the $x-y$ plane indicative of a vertically oriented magnetic dipole mode.

In Figure 3e, we depict the calculated spectra of absorption by a metasurface consisting of resonators with a diameter of 320 nm excited by a plane wave incident at different polar angles. We consider two planes of the incidence: along $\varphi = 0°$ and along $\varphi = 45°$. One can note a sharp (quality factor is 100) dispersive resonance around 1200 nm corresponding to the excitation of the out-of-plane dipole modes. Indeed, the field profiles shown in Figure 3c,d correspond to the resonance marked with a black circle. As it was discussed above, the resonance cannot be excited by a normally incident plane wave. In addition, we observe that the resonance wavelength shifts with increasing polar angle of incidence. This effect is not observed for a single nanocylinder and is due to the periodic arrangement that affects its dispersion.

PHOTOLUMINESCENCE FROM BROKEN-SYMMETRY METASURFACES

In order to further enhance photoluminescence emission, we now embed QD emitters within broken-symmetry dielectric metasurfaces[32] in which a corner has been removed from the resonator. This reduction of symmetry causes the bright, in-plane, dipole modes and dark out-of-plane dipole modes to couple, resulting in a Fano-like behavior.[32] Importantly, this allows direct coupling to the high-Q dark mode with normally incident light. Figure 4a shows a schematic diagram of the metasurface with the embedded QDs and the corresponding simulated reflectivity for normally incident light. The two sharp dips in reflectivity correspond to the high-Q dark modes.[32] Figure 4b,c show the simulated electrical fields in an $x-y$ plane midway through the resonator. The circulating electric field of the longer wavelength resonance is similar to that seen in Figure 3c and is indicative of a z-axis oriented magnetic dipole mode. The shorter wavelength resonance corresponds to a z-axis oriented electric dipole mode.

Broken-symmetry metasurfaces were fabricated using the same processes as the symmetric metasurfaces described

DOI: 10.1021/acs.nanolett.8b02808
Nano Lett. XXXX, XXX, XXX−XXX

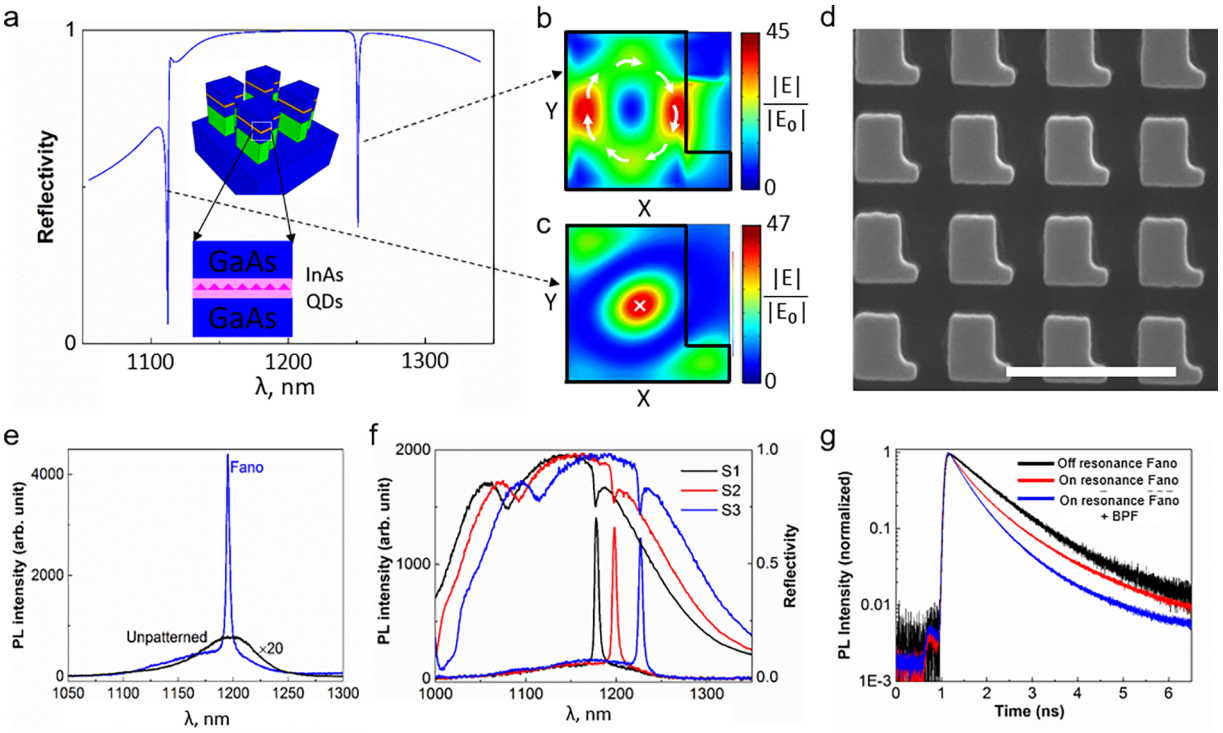

Figure 4. (a) Numerically calculated normal-incidence reflectance spectrum of the symmetry-broken metasurface for 345 nm side dimension, cut dimension is 90 nm by 240 nm, thickness is 400 nm, the boundary of the resonator is shown in panels b and c. The inset shows a sketch of the metasurface geometry. (b,c) Corresponding calculated mode profiles of the two high-Q resonant modes observed in panel a, showing the modulus of the electric field in a $x-y$ plane through the nanoresonator center. (d) Top-view scanning electron micrograph of a typical symmetry-broken metasurface sample (the scale bar corresponds to 1 μm). (e) Experimentally measured room-temperature linear-optical photoluminescence spectra for the symmetry-broken metasurface sample with a nominal side length of ∼330 nm, and a smaller cuboid notch with side dimensions of $x \sim 90$ nm and $y \sim 235$ nm cutting through the resonator. (f) Experimentally measured room-temperature linear-optical reflectance and corresponding photoluminescence spectra for three symmetry-broken metasurface samples, which differ in scaling factors. (g) Measured time-resolved low-temperature photoluminescence spectra of a sample with a smaller scaling factor because the PL peak wavelength blue shifts to ∼1110 nm at 4 K. The red curve includes emission over the full spectral range of emission of the metasurface, the blue curve shows data collected using a band-pass filter (∼10 nm fwhm, central wavelength = 1100 nm) centered around the 1100 nm resonance of the metasurface, the black curve shows data from the unstructured QD layer for reference.

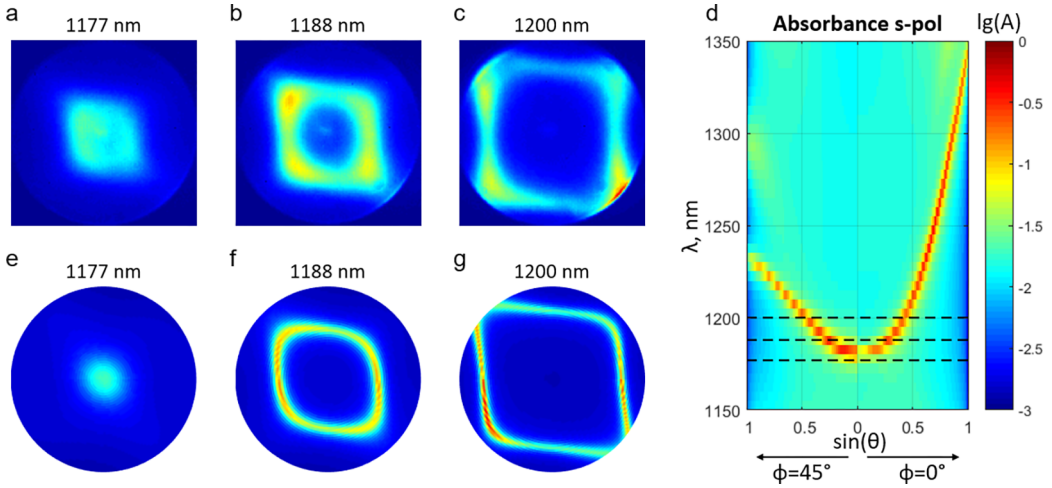

Figure 5. (a–c) Experimentally measured back-focal plane images of emission from the symmetry broken sample corresponding to the sample S2 in Figure 4f for pass bands (fwhm 10 nm) centered around 1177, 1188, and 1200 nm, respectively. The bright circle in each image corresponds to the NA of 0.65 used in experiments. (d) Numerically calculated angle-dependent absorbance spectra of a symmetry-broken sample (parameters: period 610 nm, width 330 nm, height 400 nm, cut corner footprint 250 nm × 100 nm) for s-polarized light. The dashed lines show the isofrequency slices used for calculation of the back focal plane images. (e–g) Numerically calculated back-focal plane images corresponding to the experimental images shown in panels a–c.

earlier. Figure 4d shows a top-view SEM image of a typical metasurface. These metasurfaces included only a single layer of InAs QDs. An exemplary photoluminescence spectrum, obtained when the out-of-plane magnetic dipole resonance

DOI: 10.1021/acs.nanolett.8b02808
Nano Lett. XXXX, XXX, XXX−XXX

overlaps the maxima of the QD photoluminescence band, is shown in Figure 4e. It shows a ∼110-fold enhancement of the photoluminescence peak intensity compared with an unpatterned sample, despite a filling fraction of the resonators of only ∼38%. The spectral location of this peak coincides with a sharp dip in the measured reflectivity (see Figure 4f). The measured and simulated reflectivity spectra also show a second Fano resonance at shorter wavelengths. However, the brightness enhancement at this resonance is not as large as that of the longer wavelength Fano resonance (see Supplementary Figure S2). This is likely due to the lower quality factor of the shorter wavelength resonance as evidenced by the broader spectral line width.

Photoluminescence enhancement caused by coupling to high density-of-states modes is typically accompanied by an increase in radiative rate.[36−38] To further investigate this behavior, we measured the corresponding time-resolved photoluminescence spectra from the symmetry broken metasurface samples (see Methods). The measurements were performed at ∼4 K, which significantly lengthens the lifetime of the QD photoluminescence to ∼1 ns. In Figure 4g, we compare the temporal evolution of the photoluminescence of the broken-symmetry metasurface with that of a sample with resonance outside the gain region of the QDs. A reduction of the photoluminescence lifetime is clearly observed for the metasurface sample, and an even further reduction of the lifetime is observed when the photoluminescence is collected through a 10 nm bandpass filter centered at the sharp photoluminescence peak. Indeed, as was mentioned above, the lifetime of the emission from the broken-symmetry metasurface sample off-resonance is ∼1 ns. This lifetime is reduced by a factor of ∼2 for the emission for the same sample when on-resonance. However, because of the nonradiative recombination channels for the QDs, it is not feasible to define a Purcell enhancement by directly comparing the lifetime reduction.

FAR-FIELD EMISSION ENGINEERING USING METASURFACES INCORPORATING QUANTUM EMITTERS

We now turn our attention to the use of metasurfaces with embedded emitters for engineering the far-field emission pattern. We recorded the photoluminescence angular distribution using a back focal plane (BFP) setup (see Methods). Figure 5a−c show the measured BFP images obtained from the broken-symmetry metasurfaces corresponding to Figure 4e for three differently centered passbands. The angular emission pattern of the photoluminescence, which is enhanced by coupling to the formerly symmetry protected mode exhibits a pronounced dependence on the emission wavelength. At 1177 nm wavelength, the emission is directed in a narrow cone at normal direction out of the substrate plane. At 1188 nm wavelength, the emission forms a rhombically shaped ring in momentum space, which approximately preserves its shape but becomes larger when further increasing the wavelength to 1200 nm.

To explain these observations, we calculated wave-vector-dependent absorbance spectra of the broken symmetry metasurface as described in the Methods section (see Figure 5d). The symmetry-protected mode features a characteristic U-shaped dispersion. By reciprocity, the angular dependence of the emission will correspond to that of the absorption. As seen in Figure 5d, emission normal to the substrate plane occurs at ∼1177 nm, whereas for longer wavelengths the emission shifts to larger angles, in a manner consistent with the calculated band structure. Flat regions of the bands result in higher brightness enhancement for collection with a finite-NA objective. The curvature of this dispersion can be adjusted by geometrical factors such as resonator geometry and pitch (see Supplementary Figure S3).

To allow for a more direct comparison with measured BFP images, we performed single wavelength absorbance calculations for incident wave vectors mapping the entire numerical aperture of the collection objective used in the experiment (NA = 0.65). Figure 5e−g show the simulated BFP images for wavelengths of 1177, 1188, and 1200 nm, respectively. Each calculated BFP image corresponds to one of the isofrequency slices shown in Figure 5d as dashed lines. We obtain a good agreement with the experimental BFP images. In particular, the calculated BFP images nicely reproduce the rhombical shape as well as its trend of expansion with increasing wavelength.

The collection efficiency for emission from the unpatterend wafer is below 2% for a 0.4 NA objective in the considered wavelength range. According to our numerical calculations, this value is typically enhanced by a factor of 2−7 for the broken-symmetry metasurface on-resonance depending on the exact sample parameters and wavelength considered. Thus, both the spatial redistribution of the emission and the enhanced emission rate contribute to the enhanced photoluminescence signal.

CONCLUSIONS AND OUTLOOK

To summarize, we demonstrated photoluminescence enhancement and directional reshaping of emission by monolithically embedding self-assembled near-infrared QDs within Mie-resonant III−V semiconductor metasurfaces. This manipulation of the QD photoluminescence properties is achieved by coupling their emission to high-quality-factor Mie-type resonances, which are characterized by an out-of-plane magnetic dipole moment. The far-field emission pattern can be dramatically changed by controlling the symmetry of the resonators comprising the metasurface; this symmetry is used to control the coupling between in-plane and out-of-plane dipole modes. We obtained significant brigthness enhancement (up to 2 orders of magnitude) when the QD photoluminescence spectrum overlaps high density of states modes near $k = 0$ corresponding to emission normal to the metasurface. Our results demonstrate that semiconductor metasurfaces incorporating efficient emitters can act as monolithic flat sources of light fields with spectral and directional properties tailored by the metasurface design. Based on these findings, we believe that our results open interesting opportunities for applications in smart solid-state lighting, ultraflat light sources, light-field display technology, or as complex light-field sources (e.g., for spatial multiplexing).

The monolithic semiconductor platform is especially promising regarding the future development of electrically driven metasurface light sources because many concepts from existing optoelectronic devices such as III−V semiconductor lasers and LEDs will be directly transferable to monolithic light-emitting metasurfaces. Note that while our experiments were performed at near-infrared wavelengths, our approach is, in principle, fully scalable from visible to mid-infrared frequencies. Prospectively, it will be especially interesting to investigate coupling of the out-of-plane dipole modes of the metasurfaces to intersubband transitions, which selectively emit and absorb out-of-plane polarized photons, or even to

DOI: 10.1021/acs.nanolett.8b02808
Nano Lett. XXXX, XXX, XXX−XXX

magnetic emitters. Strongly reducing the area density of the QDs may furthermore allow for the realization of a new type of quantum light sources emitting single photons with tailorable properties.

METHODS

Absorption Calculation. To calculate the angular-resolved absorption spectra of the periodic structures, we used the Fourier Modal Method. A small imaginary part is added to the refractive index of the nanoresonators material, allowing us to employ the reciprocity principle to link the calculated spectra directly to the emission characteristics of the respective structures. In Figure 1, the refractive index of the resonators was set to 5 + 0.001i, and the resonators are assumed to be surrounded by air. We used a decomposition into 25*25*2 modes. In our calculations, the plane wave is incident onto the structure at the polar angle θ, which was varied from 0° to 90°. For the calculation of Figure 3 and Figure 5, a constant absorption coefficient of $k = 0.0031$, where k is the imaginary part of the refractive index, is assumed for the nanoresonator material. For the symmetric structure, we also rigorously simulated the layered wafer with five layers of InAs inside the GaAs resonators. The results showed no notable difference as compared to the simulations of the homogeneous GaAs resonators with additional "averaged" loss factor. Therefore, here we present simulations of homogeneous GaAs resonators only.

QDs Epitaxial Growth. The samples discussed in this study were grown in a VG V80 molecular beam epitaxy (MBE) reactor on epi-ready semi-insulating GaAs (001). The substrate temperature is measured using an optical pyrometer. Prior to growth, the native oxide on the GaAs substrate is thermally desorbed at 630 °C for 20 min, following which a 200 nm thick smoothing layer of GaAs is grown at 580 °C. Next, a 500 nm thick $Al_{0.85}Ga_{0.15}As$ layer is grown at 580 °C. The substrate temperature is then brought down to 475 °C for the growth of the active medium. The QDots are formed by growing 2.5 ML of InAs on a 1 nm $In_{0.15}Ga_{0.85}As$ bottom quantum well and are ∼30 nm wide by ∼5 nm high and have an areal density of ∼2 × $10^{10}cm^{-2}$ (confirmed with AFM). The Reflection High-Energy Electron Diffraction (RHEED) clearly shows a Chevron pattern indicating the formation of QDots. They are then capped by a 4 nm thick $In_{0.15}Ga_{0.85}As$ top quantum well followed by a 1.5 nm cold GaAs cap. The substrate temperature is then brought back up to 580 °C where the rest of the GaAs cap is grown. This process is repeated for each stack of dots in a quantum well (DWELL).[33,34,39] The In and Ga growth rates were kept constant at 0.05 and 0.3 ML/sec, and a constant As:Ga ratio of 13 is maintained. The internal quantum efficiency of the three layers of DWELLs is ∼53%.

Metasurface Fabrication. The wafers were epitaxially grown by MOCVD on a semi-insulating GaAs substrate; the stack consisted of (bottom to top) a 500 nm thick $Al_{0.85}Ga_{0.15}As$ layer in the middle followed by a 400 nm thick GaAs layer with one or more layers of embedded InAs QDs. The metasurfaces were then fabricated using standard electron-beam lithography to form etch masks, followed by inductively coupled plasma etch and finished with a selective wet oxidation step that turns the $Al_{0.85}Ga_{0.15}As$ layer into an oxide and leaving the active GaAs/QDs region surrounded by low index layers or air.

Micro Photoluminescence Measurements. We optically pumped the sample using a pulsed laser with a temporal width of ∼120 fs, wavelength of $\lambda \sim 750$ nm and a repetition rate of 80 MHz. A 20× Mitutoyo near-IR objective with low numerical aperture of 0.4 was used to focus ∼5 μW pump power onto the metasurfaces that were kept at room temperature. The same objective was used to collect the photoluminescence which was subsequently measured using a near-infrared spectrometer connected to a liquid nitrogen cooled InGaAs detector array.

Time-Resolved Photoluminescence Measurements. The lifetime of the PL shown in Figure 4g was measured using a micro-PL setup (used an IR objective with NA = 0.65) that collected the emission signal, which is then directed into a liquid Helium cooled superconducting nanowire detector. The detector is capable of resolving sub-100 ps lifetime with low temporal jitter. The broken-symmetry metasurface sample was optically pumped by $\lambda = 800$ nm femtosecond pulses with an average pump power of <1 μW. The sample was kept at 4 K to significantly reduce the nonradiative rate and increase the PL lifetime to ∼1 ns. A tunable spectral filter with a bandwidth of ∼10 nm was used to spectrally select the PL measured by the detector.

Back Focal-Plane Measurements. A continuous-wave laser emitting at 532 nm wavelength was used for the excitation. The laser was focused onto the sample by a 0.65 NA (Olympus LCPLN50XIR 50×) objective. The same objective was collecting the emitted light in reflection, which then propagated through a dedicated lens system to an InGaAs camera (2D-OMA V). The residual laser light was filtered out by a long-pass dichroic mirror. The lens system was adjusted to form the back focal plane image at the sensor of the camera. A bandpass filter (Thorlabs FB1200−10) with center wavelength of 1200 nm and a passband width of 10 nm was used to selectively probe the emission in the spectral range of interest. The variation of the center wavelength of the passband was realized via tilting of the filter.

ASSOCIATED CONTENT

Supporting Information

The Supporting Information is available free of charge on the ACS Publications website at DOI: 10.1021/acs.nanolett.8b02808.

Extended discussion of the geometries of the two different types of resonator arrays and additional computational details for the results shown in Figure 1, simulated reflectance spectrum of a cylinder resonator array excited by a plane wave, measured reflectivity and PL spectra of a broken-symmetry metasurface that show brigthness enhancement at both Fano resonances, out-of-plane magnetic dipole mode dispersion for different periods (PDF)

AUTHOR INFORMATION

Corresponding Author

*E-mail: ibrener@sandia.gov.

ORCID

Sheng Liu: 0000-0001-5644-7715
Aleksandr Vaskin: 0000-0002-3014-1002
Polina P. Vabishchevich: 0000-0003-0795-2314
George Wang: 0000-0001-9007-0173
Xiaowei He: 0000-0002-4982-8250
Nicolai F. Hartmann: 0000-0002-4174-532X

DOI: 10.1021/acs.nanolett.8b02808
Nano Lett. XXXX, XXX, XXX−XXX

Han Htoon: 0000-0003-3696-2896
Stephen K. Doorn: 0000-0002-9535-2062
Isabelle Staude: 0000-0001-8021-572X
Igal Brener: 0000-0002-2139-5182

Notes

The authors declare no competing financial interest.

■ ACKNOWLEDGMENTS

This work was supported by the U.S. Department of Energy, Office of Basic Energy Sciences, Division of Materials Sciences and Engineering and performed, in part, at the Center for Integrated Nanotechnologies, an Office of Science User Facility operated for the U.S. Department of Energy (DOE) Office of Science. Sandia National Laboratories is a multimission laboratory managed and operated by National Technology and Engineering Solutions of Sandia, LLC, a wholly owned subsidiary of Honeywell International, Inc., for the U.S. Department of Energy's National Nuclear Security Administration under contract DE-NA0003525. This paper describes objective technical results and analysis. Any subjective views or opinions that might be expressed in the paper do not necessarily represent the views of the U.S. Department of Energy or the United States Government. A.V. and I.S. gratefully acknowledge financial support from the German Research Foundation (STA 1426/2-1) and by the Thuringian State Government through its ProExcellence Initiative (ACP^{2020}). X.H., Y.K., N.F.H., H.H., and S.K.D. acknowledge partial support by the Los Alamos National Laboratory Directed Research and Development Fund.

■ REFERENCES

(1) Purcell, E. M. Spontaneous Emission Probabilities at Radio Frequencies. *Phys. Rev.* **1946**, *69*, 681.
(2) Peter, E.; Senellart, P.; Martrou, D.; Lemaître, A.; Hours, J.; Gérard, J. M.; Bloch, J. Exciton-Photon Strong-Coupling Regime for a Single Quantum Dot Embedded in a Microcavity. *Phys. Rev. Lett.* **2005**, *95* (6), 067401.
(3) Ellis, B.; Mayer, M. A.; Shambat, G.; Sarmiento, T.; Harris, J.; Haller, E. E.; Vučković, J. Ultralow-threshold electrically pumped quantum-dot photonic-crystal nanocavity laser. *Nat. Photonics* **2011**, *5* (5), 297−300.
(4) Aoki, K.; Guimard, D.; Nishioka, M.; Nomura, M.; Iwamoto, S.; Arakawa, Y. Coupling of quantum-dot light emission with a three-dimensional photonic-crystal nanocavity. *Nat. Photonics* **2008**, *2* (11), 688−692.
(5) Zhen, B.; Hsu, C. W.; Lu, L.; Stone, A. D.; Soljačić, M. Topological Nature of Optical Bound States in the Continuum. *Phys. Rev. Lett.* **2014**, *113* (25), 257401.
(6) Lepetit, T.; Kanté, B. Controlling multipolar radiation with symmetries for electromagnetic bound states in the continuum. *Phys. Rev. B: Condens. Matter Mater. Phys.* **2014**, *90* (24), 241103.
(7) Zhen, B.; Chua, S.; Lee, J.; Rodriguez, A.; Liang, X.; Johnson, S.; Joannopoulos, J.; Soljacic, M.; Shapira, O. Enabling enhanced emission and low-threshold lasing of organic molecules using special Fano resonances of macroscopic photonic crystals. *Proc. Natl. Acad. Sci. U. S. A.* **2013**, *110*, 13711−13716.
(8) Akselrod, G. M.; Argyropoulos, C.; Hoang, T. B.; Ciracì, C.; Fang, C.; Huang, J.; Smith, D. R.; Mikkelsen, M. H. Probing the mechanisms of large Purcell enhancement in plasmonic nanoantennas. *Nat. Photonics* **2014**, *8* (11), 835−840.
(9) Russell, K. J.; Liu, T.-L.; Cui, S.; Hu, E. L. Large spontaneous emission enhancement in plasmonic nanocavities. *Nat. Photonics* **2012**, *6* (7), 459−462.
(10) Tanaka, K.; Plum, E.; Ou, J. Y.; Uchino, T.; Zheludev, N. I. Multifold Enhancement of Quantum Dot Luminescence in Plasmonic Metamaterials. *Phys. Rev. Lett.* **2010**, *105* (22), 227403.
(11) Kinkhabwala, A.; Yu, Z.; Fan, S.; Avlasevich, Y.; Müllen, K.; Moerner, W. E. Large single-molecule fluorescence enhancements produced by a bowtie nanoantenna. *Nat. Photonics* **2009**, *3* (11), 654−657.
(12) Muskens, O. L.; Giannini, V.; Sánchez-Gil, J. A.; Gómez Rivas, J. Strong Enhancement of the Radiative Decay Rate of Emitters by Single Plasmonic Nanoantennas. *Nano Lett.* **2007**, *7* (9), 2871−2875.
(13) Regmi, R.; Berthelot, J.; Winkler, P. M.; Mivelle, M.; Proust, J.; Bedu, F.; Ozerov, I.; Begou, T.; Lumeau, J.; Rigneault, H.; et al. All-Dielectric Silicon Nanogap Antennas To Enhance the Fluorescence of Single Molecules. *Nano Lett.* **2016**, *16* (8), 5143−5151.
(14) Bouchet, D.; Mivelle, M.; Proust, J.; Gallas, B.; Ozerov, I.; Garcia-Parajo, M. F.; Gulinatti, A.; Rech, I.; De Wilde, Y.; Bonod, N.; et al. Enhancement and Inhibition of Spontaneous Photon Emission by Resonant Silicon Nanoantennas. *Phys. Rev. Appl.* **2016**, *6* (6), 064016.
(15) Arbabi, A.; Horie, Y.; Bagheri, M.; Faraon, A. Dielectric metasurfaces for complete control of phase and polarization with subwavelength spatial resolution and high transmission. *Nat. Nanotechnol.* **2015**, *10* (11), 937−943.
(16) Jahani, S.; Jacob, Z. All-dielectric metamaterials. *Nat. Nanotechnol.* **2016**, *11* (1), 23−36.
(17) Khorasaninejad, M.; Chen, W. T.; Devlin, R. C.; Oh, J.; Zhu, A. Y.; Capasso, F. Metalenses at visible wavelengths: Diffraction-limited focusing and subwavelength resolution imaging. *Science* **2016**, *352* (6290), 1190−1194.
(18) Kuznetsov, A. I.; Miroshnichenko, A. E.; Brongersma, M. L.; Kivshar, Y. S.; Luk'yanchuk, B. Optically resonant dielectric nanostructures. *Science* **2016**, *354* (6314), aag2472.
(19) Staude, I.; Miroshnichenko, A. E.; Decker, M.; Fofang, N. T.; Liu, S.; Gonzales, E.; Dominguez, J.; Luk, T. S.; Neshev, D. N.; Brener, I.; et al. Tailoring Directional Scattering through Magnetic and Electric Resonances in Subwavelength Silicon Nanodisks. *ACS Nano* **2013**, *7* (9), 7824−7832.
(20) Staude, I.; Schilling, J. Metamaterial-inspired silicon nanophotonics. *Nat. Photonics* **2017**, *11* (5), 274−284.
(21) Zhao, Q.; Zhou, J.; Zhang, F.; Lippens, D. Mie resonance-based dielectric metamaterials. *Mater. Today* **2009**, *12* (12), 60−69.
(22) Langguth, L.; Punj, D.; Wenger, J.; Koenderink, A. F. Plasmonic Band Structure Controls Single-Molecule Fluorescence. *ACS Nano* **2013**, *7* (10), 8840−8848.
(23) Staude, I.; Khardikov, V. V.; Fofang, N. T.; Liu, S.; Decker, M.; Neshev, D. N.; Luk, T. S.; Brener, I.; Kivshar, Y. S. Shaping Photoluminescence Spectra with Magnetoelectric Resonances in All-Dielectric Nanoparticles. *ACS Photonics* **2015**, *2* (2), 172−177.
(24) Vaskin, A.; Bohn, J.; Chong, K. E.; Bucher, T.; Zilk, M.; Choi, D.-Y.; Neshev, D. N.; Kivshar, Y. S.; Pertsch, T.; Staude, I. Directional and Spectral Shaping of Light Emission with Mie-Resonant Silicon Nanoantenna Arrays. *ACS Photonics* **2018**, *5* (4), 1359−1364.
(25) Bohn, J.; Bucher, T.; Chong, K. E.; Komar, A.; Choi, D.-Y.; Neshev, D. N.; Kivshar, Y. S.; Pertsch, T.; Staude, I. Active Tuning of Spontaneous Emission by Mie-Resonant Dielectric Metasurfaces. *Nano Lett.* **2018**, *18* (6), 3461−3465.
(26) Ha, S. T.; Fu, Y. H.; Emani, N. K.; Pan, Z.; Bakker, R. M.; Paniagua-Domínguez, R.; Kuznetsov, A. I. Directional lasing in resonant semiconductor nanoantenna arrays. *Nature* https://www.nature.com/articles/s41565-018-0245-5. Published Online: Aug 20, 2018.
(27) Rutckaia, V.; Heyroth, F.; Novikov, A.; Shaleev, M.; Petrov, M.; Schilling, J. Quantum Dot Emission Driven by Mie Resonances in Silicon Nanostructures. *Nano Lett.* **2017**, *17* (11), 6886−6892.
(28) Yuan, S.; Qiu, X.; Cui, C.; Zhu, L.; Wang, Y.; Li, Y.; Song, J.; Huang, Q.; Xia, J. Strong Photoluminescence Enhancement in All-Dielectric Fano Metasurface with High Quality Factor. *ACS Nano* **2017**, *11* (11), 10704−10711.

DOI: 10.1021/acs.nanolett.8b02808
Nano Lett. XXXX, XXX, XXX−XXX

(29) Dominec, F.; Kadlec, C.; Němec, H.; Kužel, P.; Kadlec, F. Transition between metamaterial and photonic-crystal behavior in arrays of dielectric rods. *Opt. Express* **2014**, *22* (25), 30492−30503.
(30) Ko, Y. H.; Magnusson, R. Wideband dielectric metamaterial reflectors: Mie scattering or leaky Bloch mode resonance? *Optica* **2018**, *5* (3), 289−294.
(31) Rybin, M. V.; Filonov, D. S.; Samusev, K. B.; Belov, P. A.; Kivshar, Y. S.; Limonov, M. F. Phase diagram for the transition from photonic crystals to dielectric metamaterials. *Nat. Commun.* **2015**, *6*, 10102.
(32) Campione, S.; Liu, S.; Basilio, L. I.; Warne, L. K.; Langston, W. L.; Luk, T. S.; Wendt, J. R.; Reno, J. L.; Keeler, G. A.; Brener, I.; et al. Broken Symmetry Dielectric Resonators for High Quality Factor Fano Metasurfaces. *ACS Photonics* **2016**, *3* (12), 2362−2367.
(33) Albrecht, A. R.; Rotter, T. J.; Hains, C. P.; Stintz, A.; Moloney, J. V.; Malloy, K. J.; Balakrishnan, G. Multi-watt 1.25 um quantum dot VECSEL. *Electron. Lett.* **2010**, *46* (12), 856−857.
(34) Stintz, A.; Liu, G. T.; Li, H.; Lester, L. F.; Malloy, K. J. Low-threshold current density 1.3-μm InAs quantum-dot lasers with the dots-in-a-well (DWELL) structure. *IEEE Photonics Technol. Lett.* **2000**, *12* (6), 591−593.
(35) Liu, S.; Keeler, G. A.; Reno, J. L.; Sinclair, M. B.; Brener, I. III-V Semiconductor Nanoresonators-A New Strategy for Passive, Active, and Nonlinear All-Dielectric Metamaterials. *Adv. Opt. Mater.* **2016**, *4* (10), 1457−1462.
(36) Pelton, M. Modified spontaneous emission in nanophotonic structures. *Nat. Photonics* **2015**, *9* (7), 427−435.
(37) Pelton, M.; Santori, C.; Vučković, J.; Zhang, B.; Solomon, G. S.; Plant, J.; Yamamoto, Y. Efficient Source of Single Photons: A Single Quantum Dot in a Micropost Microcavity. *Phys. Rev. Lett.* **2002**, *89* (23), 233602.
(38) Gérard, J. M.; Sermage, B.; Gayral, B.; Legrand, B.; Costard, E.; Thierry-Mieg, V. Enhanced Spontaneous Emission by Quantum Boxes in a Monolithic Optical Microcavity. *Phys. Rev. Lett.* **1998**, *81* (5), 1110−1113.
(39) Chakrabarti, S.; Stiff-Roberts, A. D.; Su, X. H.; Bhattacharya, P.; Ariyawansa, G.; Perera, A. G. U. High-performance mid-infrared quantum dot infrared photodetectors. *J. Phys. D: Appl. Phys.* **2005**, *38* (13), 2135.

DOI: 10.1021/acs.nanolett.8b02808
Nano Lett. XXXX, XXX, XXX−XXX